metals

MDPI

Article

Effect of Ultrasonic Vibration and Interpass Temperature on Microstructure and Mechanical Properties of Cu-8Al-2Ni-2Fe-2Mn Alloy Fabricated by Wire Arc Additive Manufacturing

Wei Chen [1,†], Yuhua Chen [1,*,†], Timing Zhang [1], Taotao Wen [1], Zuozhu Yin [1] and Xiaosong Feng [2]

[1] Jiangxi Key Laboratory of Forming and Joining Technology for Aerospace Components, Nanchang Hangkong University, Nanchang 330063, China; waam96@163.com (W.C.); zhangtm@nchu.edu.cn (T.Z.); 18702529802@163.com (T.W.); yinzuozhu@163.com (Z.Y.)

[2] Shanghai Aerospace Equipments Manufacturer, Shanghai 200245, China; fxsupc@163.com

* Correspondence: ch.yu.hu@163.com; Tel.: +86-133-3006-7995

† These authors contributed equally to this work.

Received: 27 December 2019; Accepted: 31 January 2020; Published: 3 February 2020

Abstract: A novel ultrasonic vibration assisted (UVA) wire arc additive manufacturing (WAAM) was used to fabricate Cu-8Al-2Ni-2Fe-2Mn alloy in this study. The effect of different interpass temperatures with and without ultrasonic vibration on the microstructural evolution and mechanical properties of the fabricated part were investigated by optical microscope (OM), scanning electron microscope (SEM), transmission electron microscope (TEM), nanoindentation, and mechanical tensile testing. The results showed that reduction of the interpass temperature without UVA treatment cannot prevent the columnar dendrites directionally growing along the deposition direction. Under the UVA treatment, the coarse columnar dendrites were broken at the interpass temperature of 400 °C, and formed a fine cellular structure with an interpass temperature of 100 °C, owing to the acoustic streaming effect and cavitation effect. In addition, globular κ_{II} phase was based on Fe_3Al and lamellar κ_{III} phase was based on NiAl distributed in the interdendritic region, whereas κ_{IV} phase (rich-Fe) were precipitated in the α-Cu matrix. The improvement of microstructural characteristics caused by UVA treatment further improved the tensile properties and nano-hardness of WAAM fabricated parts. Eventually, it is experimentally demonstrated that WAAM fabricated Cu-8Al-2Ni-2Mn-2Fe alloy can obtain high-performance at UVA process under an interpass temperature of 100 °C.

Keywords: Cu-8Al-2Ni-2Fe-2Mn alloy; wire arc additive manufacturing; ultrasonic vibration; interpass temperature; microstructure; mechanical properties

1. Introduction

Nickel-aluminum bronze (NAB) alloys have high strength and oxidation, corrosion, and wear resistance, and has been widely used in marine industries [1,2]. Furthermore, NAB alloys do not show a brittle temperature range and are useful for welding and repairing structural parts with a similar chemical composition [3]. NAB alloys are usually composed of copper (Cu), aluminum (Al), nickel (Ni), iron (Fe), and manganese (Mn) elements [4]. The addition of alloying elements improves the mechanical properties of the alloy and inhibits the formation of γ_2 phase and Al_4Cu_9, which are deleterious to corrosion resistance due to the high Al content [5]. In the casting, NAB alloys includes α-Cu matrix phase, martensitic β phase (β' phase), and four intermetallic κ phases (Fe rich κ_I, κ_{II}, κ_{IV} and Ni rich κ_{III} phases) [2,6]. The microstructure evolution under equilibrium state can be approximately described as the following four stages [2,6,7]. Firstly, the primary α-Cu phase starts

to form within the β phase around the temperature 1030 °C. Secondly, around the temperature of 930 °C, if the weight percent of Fe is greater than 5%, the large precipitates (κ_I) carry out in the β phase, and another small intermetallic globular κ_{II} phase forms with a low level of weight Fe. Thirdly, at the temperature of 800 °C, the remaining β phase is transformed into the intermetallic κ_{III} phase through the eutectoid reaction. Finally, the saturation solubility of Fe (κ_{IV} phase) will precipitate in the α-Cu matrix when the temperature falls at 860 °C. Further, the retained β′ phase may appear in the NAB alloys under quenched from 1020 °C [8]. The complex microstructure of the cast NAB alloys increases the possibility of galvanic corrosion which is held in seawater [9]. Defects such as shrinkage porosity and coarser grains are prone to appear in the cast alloys owing to their poor casting properties. These weaknesses are harmful to the mechanical and corrosion properties of components.

In recent years, wire arc additive manufacturing (WAAM) has gained considerable interest due to its high deposition rate, efficiency, full density, and low equipment cost [10]. In WAAM process, an electric arc is used as a heat source and employs either gas metal arc welding (GMAW [11]), gas tungsten arc welding (GTAW [12]) or plasma arc welding (PAW [13]) to melt the wire as the feed stock. As compared to the conventional casting, the cooling rates in WAAM are significantly higher (WAAM: 10^2K/s [14], cast: 10K/s [6]) to obtain fine grains. To data, some studies have reported the properties of NAB alloys fabricated by the WAAM. Ding et al. [15] found that the post-weld-heat-treatment further refined the microstructure. There was an improvement in tensile strength and a decrease in elongation of the deposited NiAl bronze alloy. Shen et al. [16] obtained the mechanical properties in longitudinal, transverse and normal directions of the deposited Cu-9Al-4.5Ni-3.5Fe-1.3Mn alloy. The results showed the deposit exhibits higher strength in the longitudinal and transverse direction than in the normal direction. The anisotropy of WAAM NAB alloys can be modified by quenching after 900 °C for 2 h and then tempering at 650 °C for 6 h. Dharmendra et al. [17] analyzed Cu-9Al-4Fe-4Ni-1Mn alloy were formed κ_{II} and κ_{III} phase in the interdendritic regions and precipitated κ_{IV} particles within the α-matrix. The research also predicted the heat treatments in the range of 500–600 °C may increase the strength level of WAAM NAB alloys. Above all, the properties of WAAM NAB alloys may be improved by the post heat treatment, but it also increased the energy consumption and working period of the alloy preparation.

Based on issues related to the inhomogeneity of the structure and the anisotropy properties of WAAM NAB alloys, it is essential to explore a type of supplementary means that integrates in the WAAM system to improve the alloys strength and minimize anisotropy. The acoustic nonlinear effects (including specific cavitation and acoustic streaming) arising in ultrasonic vibration can influence the convection and solidification behaviors of the molten pool [18]. Hence, ultrasonic vibration has been effectively used in melting metal solidification processes such as casting [19,20], welding [21], cladding [22], additive manufacturing [23–26]. Wang et al. [25] discovered that laser engineered net shaping of Inconel 718 with ultrasonic vibration could refine the microstructure, decrease micropore, improve homogeneity of chemical contents and shorten the size of Laves phases. Ultrasonic vibration was used to assist laser engineered net shaping to fabricate Fe-Cr stainless steel [23] and 4047 aluminum [26], which had analogous phenomena in reducing micropore and refining grains. However, there are no reported investigations on ultrasonic vibration assisted (UVA) treatment during the WAAM process of fabrication the NAB alloys parts.

In this paper, the NAB alloy (Cu-8Al-2Ni-2Fe-2Mn) fabricated by WAAM with and without UVA treatment under different interpass temperatures were studied. The changes in microstructure, elemental distribution, phase constituent, nano-hardness, and tensile properties were investigated. Moreover, the formation of microstructure and fracture characteristic were also discussed in detail.

2. Experimental Procedures

2.1. Experimental Setup

A welding machine associated with a system of ultrasonic vibration was utilized to conduct the experimental investigations. Figure 1a illustrated the experimental setup of UVA WAAM, which was composed of a weld system (Fronius Trans Puls Synergic 2700 welding machine, Fronius, Pettenbach, Austria) with a motion control system, a system of ultrasonic vibration. Ultrasonic vibration was produced by an ultrasonic generator (Jian Pai Ultrasonic Technology Co., Ltd., Dongguan, China) with a maximum 2000 W output power and 20 kHz vibration frequencies. The vibration direction was perpendicular to the substrate metal. An infrared thermometer and K type thermocouples were used to measure the in-situ interpass temperature, thereby controlling the dwell time between deposition of layers. The sampling rate of the K type thermocouple was 1 Hz and the measuring range of temperatures was between 0 and 1350 °C. In this study, the ultrasonic vibration system functioned at a power of 2000 W, and different interpass temperatures of 100 °C and 400 °C with and without ultrasonic vibration were compared (Compared with a higher temperature, a better macroscopic morphology can be obtained at the interpass temperature of 400 °C. The interpass temperature of 100 °C is selected with the purpose of avoiding the influence of heat accumulation on the microstructure and mechanical properties).

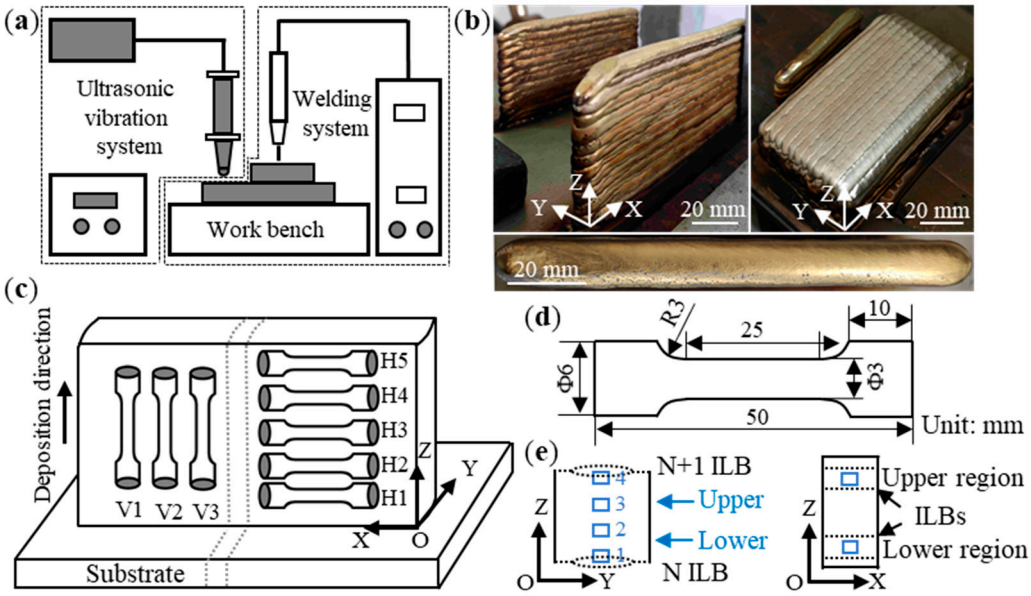

Figure 1. (**a**) Schematic diagram of the experimental apparatus of ultrasonic vibration during WAAM, (**b**) typical WAAM fabricated samples, (**c**) schematic configuration of the sample preparation, (**d**) dimensions of tensile specimens in mm, (**e**) schematic diagram of microstructure observation position.

2.2. Materials

Commercially available Cu-8Al-2Ni-2Fe-2Mn alloy wire with a diameter of 1.0 mm was employed as a filler material, of which the chemical composition was 86Cu, 8Al, 2Ni, 2Fe, and 2Mn (in wt.%) (made by Newland (Tianjin) Welding Material Co., Ltd., Tianjin, China. The substrate in the present work was a low carbon steel plate with dimensions of 180 × 100 × 6 mm^3. Before the WAAM process, the substrate surface was cleaned to remove grease and oil with acetone. Based on the preliminary experimental results, some wall samples were produced with the same welding parameter (arc current: 97 A, arc voltage: 10.3 V, welding rate: 0.48 m/min, wire feed rate: 4.0 m/min, nominal increment of Z axis: 1.8–2.2 mm, nominal increment of Y axis: 3 mm and argon flow rate 15 L/min). The deposition torch tip to work distance was kept to 15 mm, and contact angle was 90° for all the experiments.

The welding path was alternated back and forth, and the typical fabricated wall samples were presented in Figure 1b.

The single bead walls were used to study the effect of UVA and interpass temperature on the microstructure and mechanical properties. In order to ensure the integrity of the sampling and the accuracy of the results, all tested samples are deposited with a length of 120 mm and a height of not less than 50 mm. The nomenclature and processing parameters used are given in Table 1.

Table 1. The nomenclature and processing parameters of the sample.

Numbers	Interpass Temperature/°C	Ultrasonic Power/W	Number of Deposition Layers/Cycles	Height/mm	Ratio of Effective Area/%
C1	730–750	-	18	39.36	65.5
C2	Below 400	-	23	53.74	70.0
C3	Below 100	-	22	53.65	79.5
U1	710–735	2000	28	52.76	53.9
U2	Below 400	2000	26	53.68	75.9
U3	Below 100	2000	25	53.19	84.8

2.3. Characterization of Microstructure and Properties

The required specimens were machined by wire electric discharge machine (Maidenvan Machinery Co., Ltd., Nanchang, China). The specimens used for metallographic observation and nano-hardness test were cut from the center area (as shown by the dotted line in Figure 1c). A mixed solution of 5 vol.% ferric chloride, 20 vol.% hydrochloric acid, and 75 vol.% distilled water was used to reveal the microstructure of the samples after mounting, grinding and polishing. The microstructures of the samples were examined using a Zeiss Axio Scope A1 optical microscope (OM) (Carl Zeiss Microscopy GmbH, Gottingen, Germany) and Hitachi SU 1510 scanning electron microscope (SEM) (Hitachi, Tokyo, Japan). FEI Talos f200x transmission electron microscope (TEM) (FEI, Hillsboro, OR, USA) was used to identify the elemental distribution and phases constituent in the microstructure. The samples were prepared by mechanical polishing to a thickness of 50 μm followed by further thinning via ion-beam milling using a Gatan Precision Ion Polishing System (Gatan Model 691) (Gatan Inc., Sarasota, FL, USA) operating at an accelerating voltage of 200 kV for TEM study. High angle annular dark field (HAADF) detectors (FEI, Hillsboro, OR, USA) were used in combination with EDS to generate elemental maps. Selective area diffraction was used to obtain patterns from the α-Cu matrix and interdendritic region, respectively.

To study the tensile behavior, cylindrical tensile samples 3 mm in diameter were extracted from the deposited wall, along the vertical direction and the horizontal direction. Hereinafter, the two orientations were referred to as V and H, respectively. The location and size of the tensile specimens were shown in Figure 1c,d. The comparison of tensile properties between the H and V direction was investigated. Considering the heterogeneous mechanical properties within the fabricated component [27], five specimens were machined in different horizontal regions to reveal the effects of location on the tensile properties (as shown in Figure 1c). In addition, a reference cast NAB sample, which was close to the composition of the welding wire, was used to test the tensile properties. The cast NAB specification corresponded to UNS C95220 and the nominal composition (in wt.%) of this material was: Cu: 81% minimum, Al: 8.0–10.5%, Ni: 2.5%, Fe: 2.0–4.0%, Mn: 0.5–2.0%. The tensile tests were performed at room temperature with an extension rate of 0.5 mm/min using an Instron 8872 universal testing machine (Instron Corporation, Norwood, MA, USA). The strain was measured by the electronic extensometer. The fracture surfaces were examined by SEM. Nanoindentation was used to measure nano-hardness and modulus of different samples. The nano-hardness test was performed using a Nano-mechanics (Nanomechanics Inc., Oak Ridge, TN, USA) and a loading force of 50 mN at room temperature. The indenter was gradually loaded on the surface of sample within 20 s, and then kept steady for 5 s, finally unloaded gradually within 2 s. The melting points of WAAM fabricated sample

was determined by using Netzsch Sta 449F3 differential scanning calorimetry (DSC) (Netzsch, Selb, Germany) with a heating rate of 10 °C/min.

3. Results and Discussion

3.1. Macrostructure

The effect of ultrasonic vibration and interpass temperature on macrostructure is shown in Figure 2. The NAB components fabricated using the WAAM process with or without UVA treatment reached full density and no porosity defect was found in the cross-sections (C1 and U1 samples are continuous deposition with higher interpass temperature and poor forming, which are not compared in this paper). It can be found that columnar grains grow epitaxially along the deposition direction, and the interlayer bands (ILB) are clearly visible in the interpass temperature 400 °C sample (Figure 2a). The similar results are shown in the interpass temperature 100 °C samples, as the size of the columnar grains decreased, resulting in the reduction of the contrast, which made it difficult to characterize the ILB (Figure 2b). In the UVA treatment of WAAM specimens, the grain size is further refined and the deposited layer becomes wider (Figure 2c,d). The width of the thin walls increased from 7.5–8.0 mm to 8.5–9.0 mm after treatment UVA. The size of the WAAM component is decided by the shape of the molten pool [12]. The ultrasonic vibration is able to accelerate the relative movement between the solid phase and surrounding liquid phase in the molten pool, leading to a better spreading of the molten pool on the previously deposited layers. This is beneficial for increasing the effective area of deposition. A schematic diagram of the effective area of deposition is shown on the right side of the macrostructure in Figure 2, and the results are listed in Table 1. The experimental results show that the U3 sample enables the maximum deposited efficiency, reaching 84.8%.

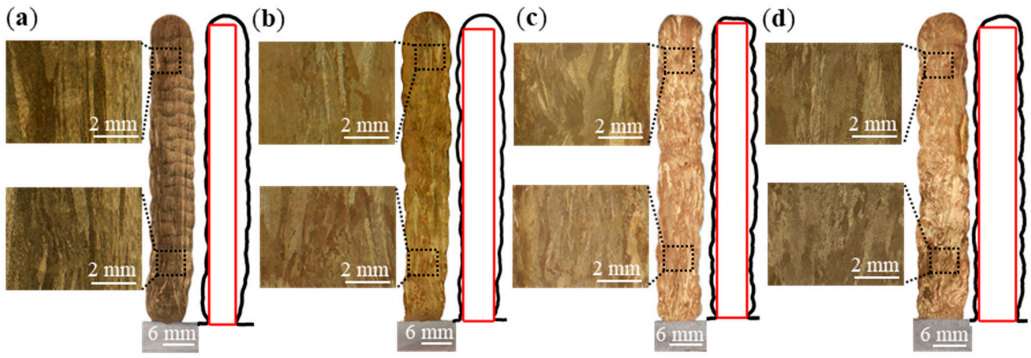

Figure 2. Morphology of Cu-8Al-2Ni-Fe-2Mn alloy with different parameters (Y-Z plane) and effective area: (**a**) sample C2, (**b**) sample C3, (**c**) sample U2, (**d**) sample U3. (The macro image on the left is an enlarged view of the position in the black dotted box).

3.2. Microstructure and Composition

Changes of the alloy's grain size are usually related to the weld processing parameters. Interestingly, the interpass temperature and ultrasonic vibration could also effectively change the microstructure of the NAB alloy during WAAM when the weld processing parameters remain unchanged. Figure 3 shows the OM micrographs of the microstructure between two adjacent ILB fabricated by WAAM in different interpass temperatures with and without UVA treatment (Y-Z plane, the observation position is shown in Figure 1e). The microstructure of the Cu-8Al-2Ni-2Fe-2Mn alloys without UVA treatment is mainly composed of columnar dendrites, as shown in Figure 3a1–a4,b1–b4. The size and morphology of the microstructure are quite different. The region of elongated columnar grains without secondary dendrite arms (SDA) growth along the deposition direction due to a high temperature gradient (G) and a slow growth rate (R) at the bottom of the molten pool delineated the ILB and is marked with a white arrow (Figure 3a1,b1). With the decrease of the temperature gradient from the bottom to the

top of the molten pool, the liquid metal becomes undercooled and leads to the destabilization of the solidification front [28], the columnar grains turn to be coarser and gradually form SDA (Figure 3a3,b3). The morphology of SDA is related to the cooling rate [29]. More SDAs are found in the samples which undergo higher interpass temperatures. In fact, at the top of each deposited layer, the epitaxial growth of the columnar dendrites structure is blocked off by a random oriented equiaxed dendrites structure, the equiaxed dendrites with a thickness of about 200–300 μm (Insert picture in Figure 4a). The transition character of the top region is revealed in a higher magnification (Figure 4a). It is believable that the columnar to equiaxed transition occurs at the top of the molten pool due to the decrease of the temperature gradient and the increase of the interface moving velocity [30]. There is no subsequent layers re-melting it, hence, only the top region shows this transition characteristic.

When the UVA treatment WAAM is under the interpass temperature of 400 °C, part of the columnar dendrites structure is fractured and the grain size is further decreased (as shown in Figure 3c1–c3). At the top of the molten pool that is near the ILB, abundant columnar dendrites with SDAs are also found (Figure 3c4). Hence, a mixed microstructure contains the coarse cellular dendrites, cellular grains and columnar dendrites, which are formed in UVA treatment WAAM samples with a higher interpass temperature. With further decrease of interpass temperature at 100 °C, the microstructure is refined to form a cellular structure and the grain boundaries are shortened (Figure 3d1–d4). Similar microstructure evolution has been reported for fabrication using laser additive manufacturing [23,25] and welding process [21,31]. Ultrasonic vibration induces acoustic streaming and cavitation caused the stirring and mixing of liquid materials in the molten pool [18,32,33]. Meanwhile, the effect of heating accumulation can be eliminated by controlling the interpass temperature. The actions of stirring and mixing lead to a homogenizing density and heat in the molten pool, which contribute to the uniform distribution of grains and the formation of a cellular structure with uniform grain boundaries.

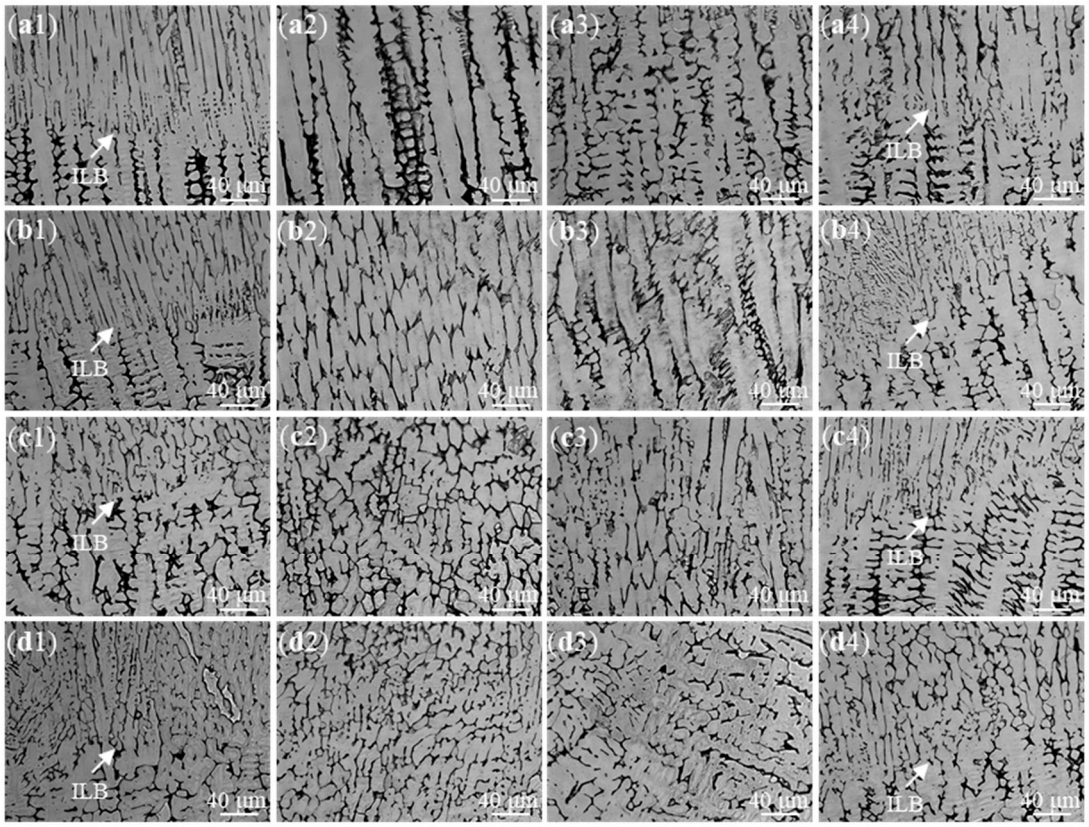

Figure 3. The microstructure between two adjacent ILB in different treatment (Y-Z plane): (**a1–a4**) sample C2, (**b1–b4**) sample C3, (**c1–c4**) sample U2, (**d1–d4**) sample U3.

The microstructure of some characteristic regions is shown in Figure 4. Figure 4b,c shows the comparisons of the deposition layers near the substrate. The C2 sample without UVA treatment presents the planar growth in the bonding interfaces due to the high temperature gradient and slow growth rate at the bottom of the molten pool near the substrate and is marked by a black arrow. With the decrease of G/R, random distribution of dendrites form into α-Cu matrix and then change to cellular structure (Figure 4c). This cellular structure grows in the opposite direction to the temperature gradient and eventually forms columnar dendrites. Similar phenomena are obtained for the C3 sample.

In comparison to the WAAM without UVA treatment (Figure 4b), the UVA treatment WAAM produces a weaker bonding interface, as shown in Figure 4d. Further, the pressure in the acoustic field made the solid-liquid interface morphologically unstable and fragmented the dendrites and epitaxial cellular tips [33]. These dendrite tips are conveyed into the undercooled melt via convection. In the meantime, a large amount of grain nucleation is formed. Hence, the alloy fabricated with UVA treatment generated equiaxed grain in a smaller grain size (about 5–12 μm) at the bottom region. It can be discerned that there exist two kinds of morphology of ILB, which is an important feature. One is that the ILB exhibit typical columnar grains orient upwards, which often shows a little darker contrast compares with the surroundings under OM (the OM insert in Figure 4e and macrostructure in Figure 2a). The higher magnification observation of the microstructure (Figure 4e,f) shows that the below ILB expresses the relatively larger primary dendrite arms (PDA) spacing with SDAs. In contrast, the secondary arms are partially re-melting in the ILB. The characteristics of ILB in the C2, C3 and U2 samples all conform to this formation rule. Other kinds of cambered bands in U3 sample shows the different size of cellular structure in ILB (Figure 4g). With the micrograph in Figure 3d1–d4, the microstructure of the U3 sample can be divided into three parts: ILB, fine cellular zone, and coarse cellular zone. The formation of ILB can be attributed to the partial re-melting of the previously deposited layers and complex thermal history experienced by the WAAM process. Zhu et al. [34] also found that the ILB were spaced uniformly in the whole sample, which demonstrated that it was just a result of the depositing layer. Furthermore, the two adjacent ILB are 2.0–2.2 mm in separation, which corresponds to the average added layer height. It is easy to measure that the deposition height of the last layer is more than 2.4 mm for the convenience of explaining the ILB are re-melting structure.

Figure 4h shows a higher magnification of interdendritic structure from U3 sample. The microstructure consists of α-Cu matrix and perishable etch interdendritic κ phase. Besides, no evidence of retain β or acicular β′ martensite is observed in the UVA treatment WAAM sample, a similar result is reported in Dharmendra's studies [17]. However, SEM and OM are difficult to qualitatively evaluate the type of the precipitation phase in the UVA treatment WAAM samples. The TEM examination is discussed in detail below.

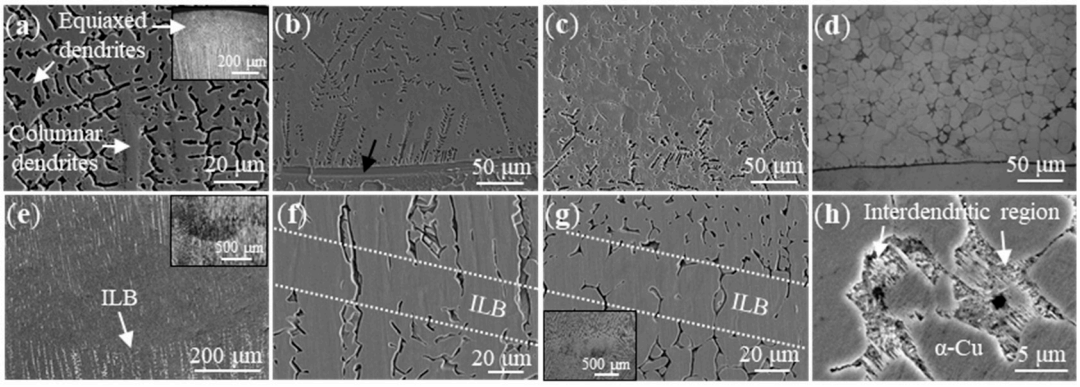

Figure 4. The microstructure of some characteristic regions (Y-Z plane): (**a**) the transition of microstructure from C2 sample, (**b**) the bottom region of C2 sample, (**c**) the dendrites transformed to cellular structure in C2 sample, (**d**) the bottom region of U3 sample, (**e**) interlayer bands (ILB region) in C2 sample, (**f**) ILB of C2 sample, (**g**) ILB of U3 sample, (**h**) interdendritic region in magnification from U3 sample.

As we know, the microstructure is very sensitive to temperature, while the different locations of the deposited wall during the WAAM process undergo rapid melting and solidification with a complex thermal history, so it is necessary to observe the microstructure in different deposited heights. Figure 5 shows the microstructure in the X-Z plane of each component is described in lower and upper regions (the location is shown in Figure 1e). All of the samples without UVA treatment have coarse columnar dendrites grown epitaxially along the deposition direction, as shown in Figure 5a–d, which accord with the observation in the Y-Z plane. Continuous columnar dendrites are blocked by UVA treatment in the U2 sample and the broken character can be seen more clearly in the high magnification SEM image (Figure 5e,f). A similar cellular structure is found in the UVA treatment at an interpass temperature of 100 °C sample (Figure 5g,h). It is important to point out that different vertical locations strongly effect PDA spacing. In the C2, C3, and U2 samples, the PDA spacing is coarsened with increasing deposition height. After analysis by the quantitative metallography method, the average PDA space of the C2, C3, U2, and U3 samples is around 28.5 ± 4.2 μm, 21.6 ± 3.6 μm, 26.8 ± 3.1 μm, and 18.6 ± 2.6 μm, respectively.

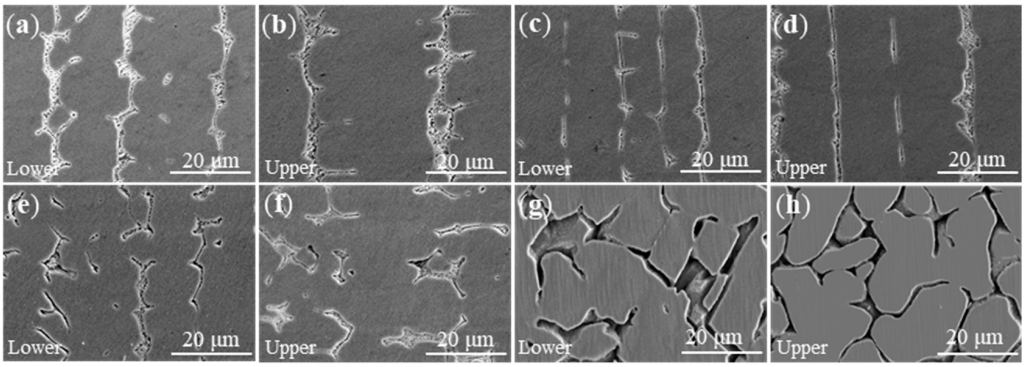

Figure 5. Effect of deposited height on microstructure in different treatment (X-Z plane): (**a**,**b**) sample C2, (**c**,**d**) sample C3, (**e**,**f**) sample U2, (**g**,**h**) sample U3.

The typical microstructure of the X-Y plane is shown in Figure 6 (the observation location is marked with a blue arrow in Figure 1e). Since the microstructure grows epitaxial along the deposition direction (i.e., Z direction) in C2, C3 and U2 samples, it appears as coarse dendritic structure in C2 due to develop SDA (Figure 6a,b). Typical equiaxed grains are found in C3 sample (Figure 6c,d) in this section, which result in fewer SDAs at lower interpass temperatures. In the cross-section of the UVA treatment samples, the size of dendritic structure is further reduced (i.e., U2 sample in Figure 6e,f), and the microstructure of the U3 sample is similar to that of the other two cross-sections (Figure 6g,h), which also proves that the microstructure form in the U3 sample is more uniform.

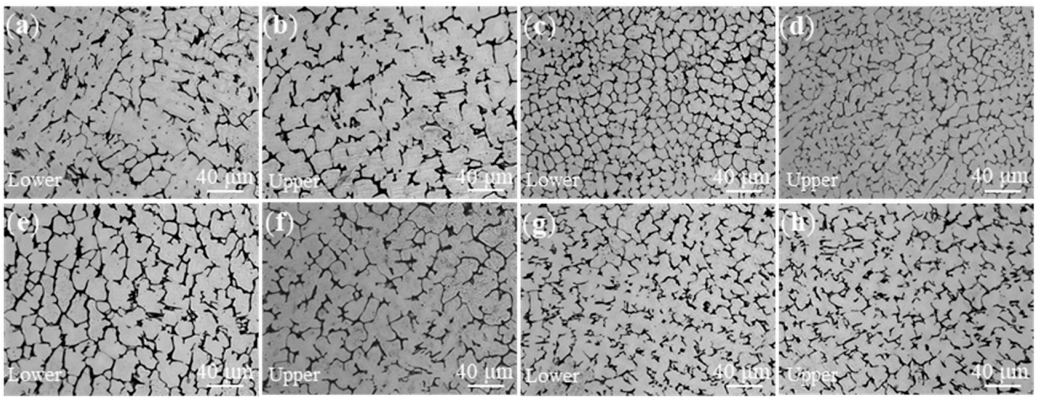

Figure 6. Effect of deposited height on microstructure in different treatment (X-Y plane): (**a**,**b**) sample C2, (**c**,**d**) sample C3, (**e**,**f**) sample U2, (**g**,**h**) sample U3.

The WAAM process involves a larger melt pool diameter and layer height than power bed technologies, which generally lead to a greater microstructural heterogeneity and more severe ILB [35]. Hence, the microstructure between two adjacent ILB changes regularly with the temperature gradient and growth rate, and the phenomenon is more obvious under the control of interpass temperature. The Cu-8Al-2Ni-2Fe-2Mn samples fabricated by WAAM without UVA treatment not only contain columnar dendrites, but also exhibit columnar to equiaxed dendrites transition. Kurz and Fisher [36] established a solid-liquid interface model for instability criterion during solidification, which pointed out the ratio of G/R determined the growth morphology and G·V controlled the scale of the microstructure formed. Bermingham [37] reported the thermal environment was dynamic during additive manufacturing and equiaxed grain formation was only achievable when temperature gradients decrease sufficiently to permit constitutional supercooling. With the decrease of G/R from the bottom to the top of the molten pool, the grain morphology might change from columnar dendrites to equiaxial dendrites due to serious constitutional undercooling. Forced control of the interpass temperature causes the deposited layer act as a mainly heat sink, which made the amounts of heat flux dissipates downward during the solidification process and results in regular changes in the microstructure between adjacent ILB.

As shown in Figure 7a, the endothermic peaks in calorimetric curve reveal the melting point of the WAAM Cu-8Al-2Ni-2Fe-2Mn alloy is about 1020 °C. The typical thermal cycle measures in the WAAM built for a sequence of six added layers is shown in Figure 7b. The first curve is the thermal cycle of thermocouple plunge into the melt pool. The peak temperature of the second curve is very close to the melting point measured by DSC. Hence, we can predict that the temperature of the arc melting pool is high enough to re-melt the equiaxed dendrites region (Figure 4a), while the SDAs help to maintain the growth direction of primary dendrites in subsequent layers (Figure 3a1–b4 and Figure 4f), and finally forms the epitaxial growth.

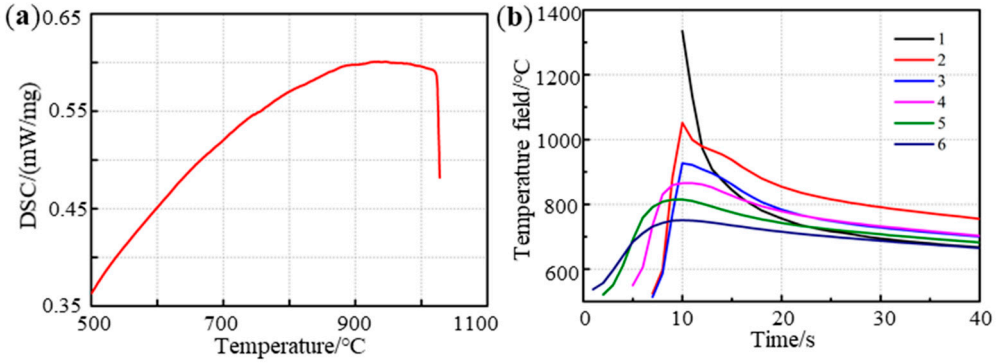

Figure 7. (**a**) DSC curve of the WAAM NAB sample, (**b**) the thermal cycle for deposited layers.

Previous studies reveal that the microstructure of materials depends on both the nucleation condition and subsequent growth stage [19,26]. The UVA treatment WAAM at lower interpass temperature can hinder the growth of epitaxial columnar more effectively and promote the formation of new grains. The refinement of the microstructures mainly results from the actions of acoustic streaming and cavitation induced by ultrasonic vibration [18,32,33]. The pressure in the acoustic streaming makes the solid-liquid interface morphologically unstable and fragments the columnar grain tips. With the assistance of instant high acoustic streaming, the primary coarse columnar grains are broken and fragmented because of the force. These dendrite tips are conveyed into the undercooled melt via convection and stirring. In the meantime, a large amount of grain nucleation is formed. With a lower interpass temperature of 100 °C, the effect of heat accumulation on the WAAM process is eliminated. Eventually, WAAM parts with refined grains are obtained UVA treatment at a lower interpass temperature process during the nucleation stage.

In order to reveal the various intermetallic phases in the interdendritic regions and α-Cu matrix, detailed TEM observations of the U3 sample were studied. Figures 8 and 9 show the distribution features of elements at the interdendritic regions and α-Cu matrix. The interdendiritic regions display two types of intermetallic phases, κ_{II} phase in the different globular sizes (Range from some nanometers to tens nanometers) and κ_{III} phase in the lamellar morphology, and EDS elemental mapping distinctly reveals the morphology (Figure 8). The κ_{II} and κ_{III} phase are found to be Fe_3Al and NiAl, respectively, based on the selected area diffraction pattern analysis, as shown in Figure 10a,b,d,e. Some amounts are very fine to the sizes of κ_{IV} phase (Fe-rich, 5 to 10 nm in size) precipitate is observed in the α-Cu matrix (Figure 9). The observation of fine Fe-rich precipitation and precipitation-free areas is distributing non-uniformly in the α-Cu matrix, which may be resulted by the different effects of thermal cycling of the WAAM on different locations. Selected area diffraction pattern analysis reveals the κ_{IV} precipitates have a composition and crystal structure is similar to that of κ_{II} based on Fe_3Al (Figure 10c,f). It is possible that the κ_{II} and κ_{IV} are being precipitated at the same temperature from the same phase [5]. The small and disperse κ_{IV} phases may inhibit grain boundary mobility, which beneficial for improving strength [38], and also preventing grain growth [4].

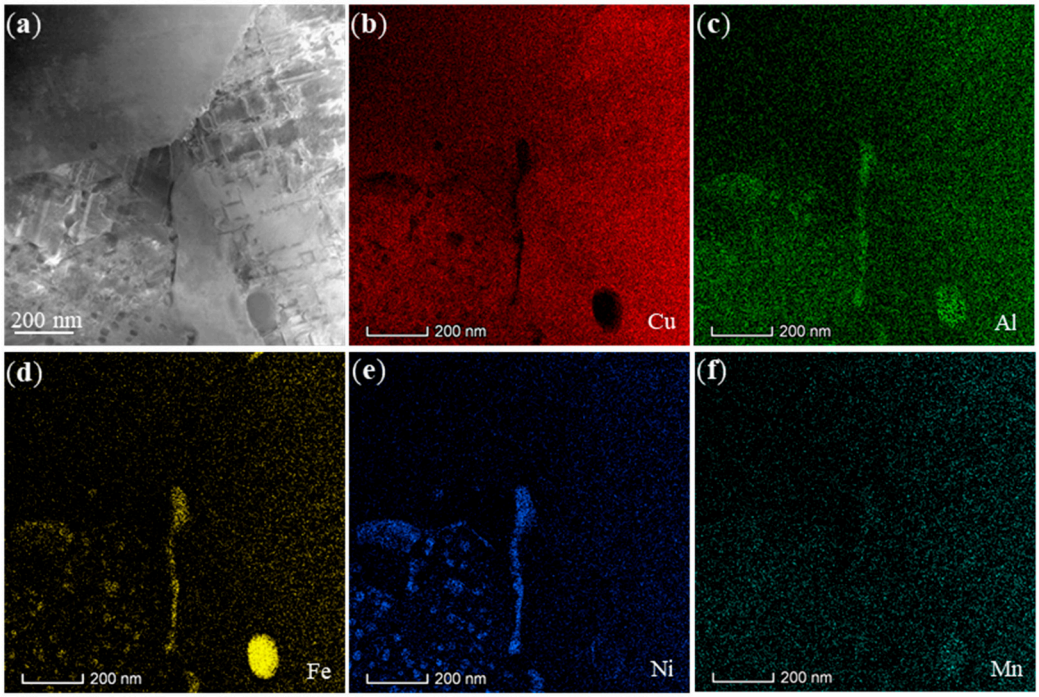

Figure 8. (**a**) HAADF image of the UVA treatment WAAM in the interdendritic region, (**b**–**f**) corresponding EDS elemental maps for Cu, Al, Fe, Ni, and Mn, respectively. The globular precipitates are Fe_3Al (κ_{II}) and the lamellar precipitates are NiAl (κ_{III}) in the interdendritic region.

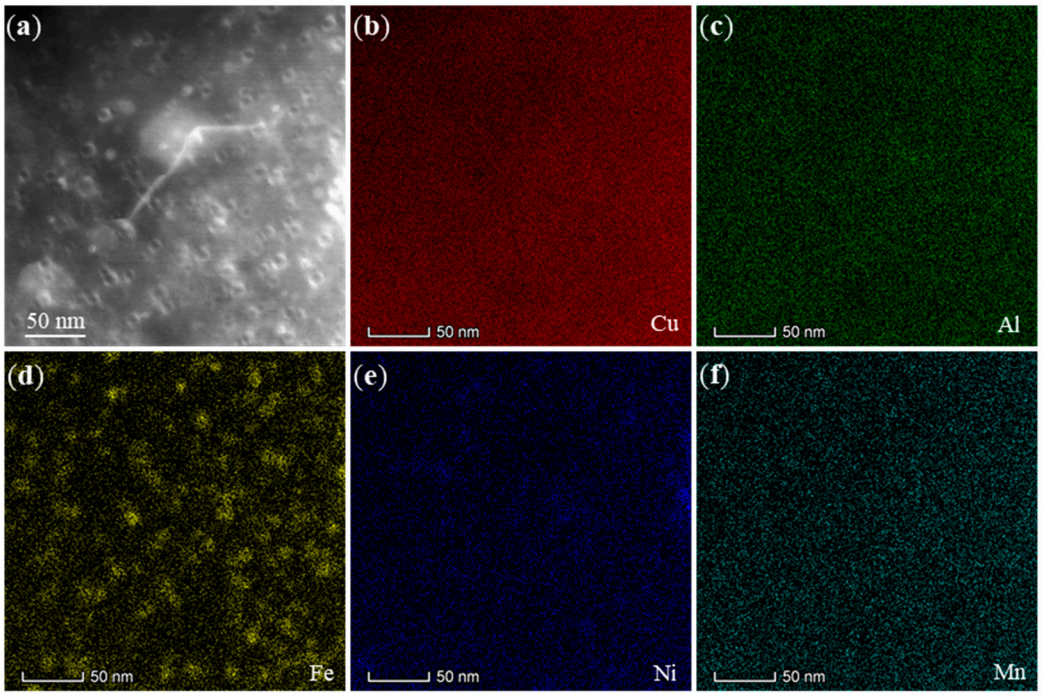

Figure 9. (**a**) HAADF image of the UVA treatment WAAM in the α-Cu matrix region, (**b**–**f**) corresponding EDS elemental maps for Cu, Al, Fe, Ni, and Mn, respectively. The precipitates are Fe-rich (κ_{IV}) in the α-Cu matrix.

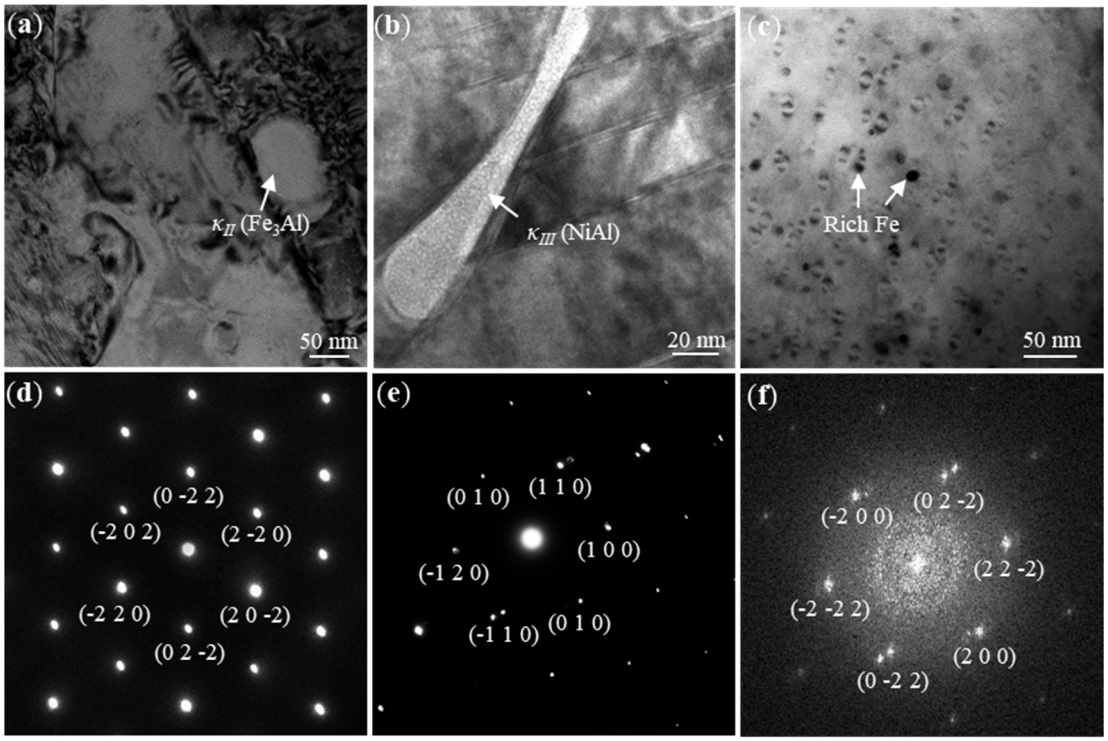

Figure 10. TEM-bright field micrographs images and selected area diffraction pattern: (**a**) κ_{II} precipitates (Fe_3Al) in the interdendritic, (**b**) κ_{III} precipitates (NiAl) in the interdendritic, (**c**) κ_{IV} precipitates (Fe-rich) in α-Cu matrix, (**d**–**f**) corresponding selected area diffraction pattern Fe_3Al, NiAl and Fe-rich, respectively.

The results of TEM observation shows that the twins and dislocations can be found near the interdendritic region of the sample with UVA treatment. In the specimen process with UVA treatment at interpass temperature of 100 °C, the coexistence of twins and interdendritic is shown in Figure 11a. The high-resolution HRTEM micrograph and corresponding selected area electron diffraction are inserted in Figure 11a, which further verifies the structure of twins. The areas between the twin bands, which are tens of nanometers in thickness, seem to be parallel to each other, and EDS elemental mapping indicates that this parallel twinning may rely on κ_{III} precipitates (NiAl) in the interdendritic region (Figure 12). Figure 11b presents a density of dislocations in the U3 sample. The dislocations form rectangular blocks of 50–120 nm in size. EDS elemental mapping reveals that there is no obvious precipitated phase in the dislocations (Figure 13). Meanwhile, the microstructure, that is without UVA treatment, specimens is simpler, as no obvious twins and dislocations occurs in the C3 specimen, as shown in Figure 11c. Hence, combining previous studies [39,40] and the results obtained in this study, it can be concluded that the action of UVA treatment WAAM solidification process can help to create twins and dislocations. The twins and dislocations may contribute to strengthening of the WAAM NAB alloy by acting as a grain boundary and blocking the lattice dislocation motion [41,42].

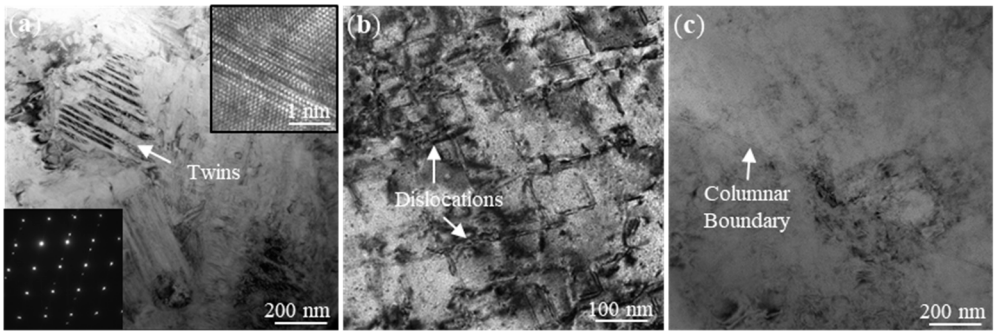

Figure 11. TEM-Bright field micrographs images: (**a**) twins from U3 sample, (**b**) dislocations from U3 sample, (**c**) α-Cu matrix with columnar grain boundary from C3 sample.

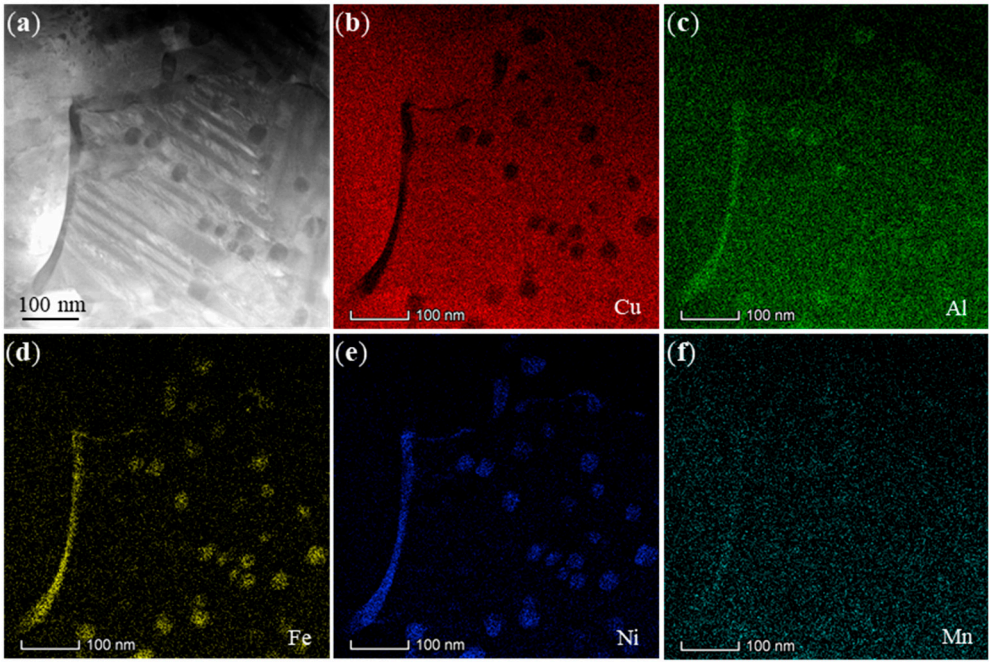

Figure 12. (**a**) HAADF image of the UVA treatment WAAM in the twinning region, (**b**–**f**) corresponding EDS elemental maps for Cu, Al, Fe, Ni, and Mn, respectively. The lamellar precipitates are NiAl (κ_{III}), and globular Fe_3Al (κ_{II}).

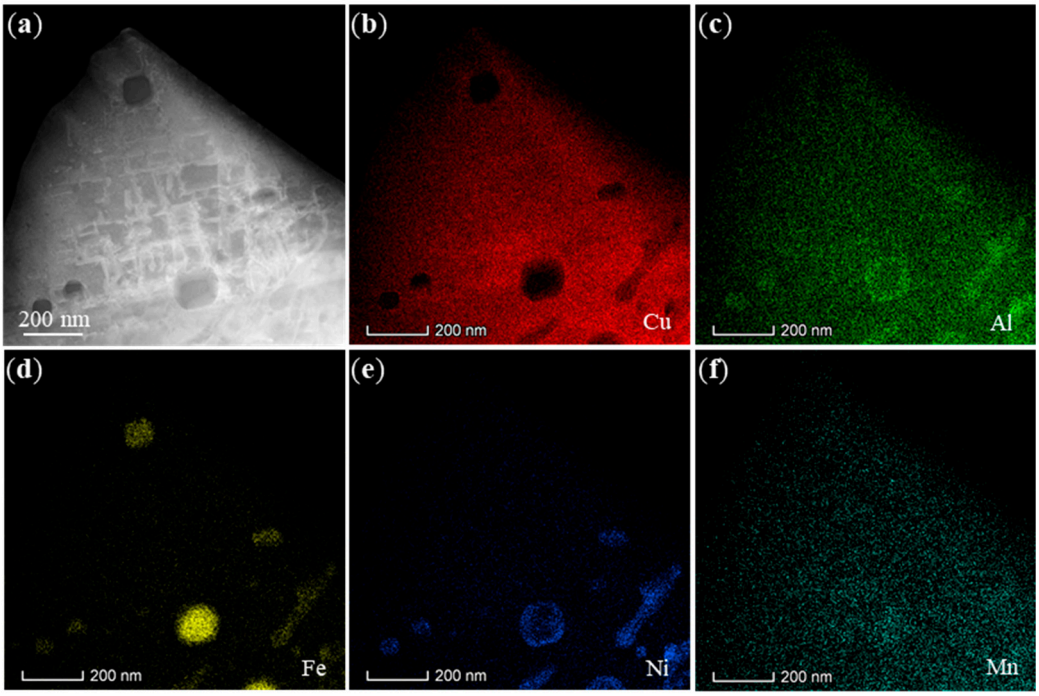

Figure 13. (**a**) HAADF image of the UVA treatment WAAM in the dislocations region, (**b**–**f**) corresponding EDS elemental maps for Cu, Al, Fe, Ni, and Mn, respectively. The lamellar precipitates are NiAl (κ_{III}), and globular Fe_3Al (κ_{II}).

3.3. Nano-Hardness and Tensile Properties

To acknowledge the variation of nano-hardness and modulus by the ultrasonic vibration and interpass temperature, the nano-indentation tests are conducted on the interdendritic region, ILB, α-Cu matrix lower and upper the ILB, respectively. Typical load-depth cures for four regions in C2, C3, U2 and U3 samples are plotted in Figure 14a–d. It can be seen that the contract depth, maximum depth and final depth in the interdendritic region are shallower than those in the α-Cu matrix and ILB, which could partly reflect a greater nano-hardness of the interdendritic region. Besides, the ILB exhibits the maximum depth, which means that the nano-hardness value of the area is the minimum. In addition, the indentation test curves indicate a good repeatability with UVA treatment under interpass temperature of 100 °C samples (Figure 14d).

The variation trends of both nano-hardness and modulus in four samples are shown in Figure 14e,f. Each position nano-hardness value represents an average of at least 8 measurements. With the interpass temperature decreasing (C3 sample) and UVA treatment under interpass temperature of 100 °C (U3 sample), the nano-hardness of α-Cu matrix and ILB is increase, and the nano-hardness in the interdendritic region is decreases (Figure 14b,d). Apart from the enhancement in nano-hardness, the modulus also slightly increases in α-Cu matrix and ILB, and decreases in the interdendritic region. It is often desirable to have more uniform nano-hardness in the material. With UVA treatment under interpass temperature of 100 °C, the nano-hardness in interdendritic region, ILB zone, the α-Cu matrix upper the ILB, the α-Cu matrix lower the ILB are 2.28 ± 0.09 GPa, 2.11 ± 0.02 GPa, 2.24 ± 0.03 GPa and 2.22 ± 0.02 GPa, while the four modulus are 129.4 ± 3.80 GPa, 122.4 ± 1.48 GPa, 126.4 ± 2.22 GPa and 126.1 ± 2.06 GPa, respectively. The nano-hardness and modulus of the WAAM Cu-8Al-2Ni-2Fe-2Mn alloy in U3 sample is relatively close, which indicates that the Cu-8Al-2Ni-2Fe-2Mn alloy fabricated by UVA treatment under interpass temperature of 100 °C is more stable. The uniform and increase of the α-Cu matrix and ILB in U3 sample is mainly attributed to two reasons: (i) based on the Hall-Petch law, the nano-hardness increases with the decreases of the grain size which is caused by UVA treatment [43]. (ii) according to the TEM results, the precipitation of κ_{IV} phase in the α-Cu matrix may increase the mean nano-hardness [17,44].

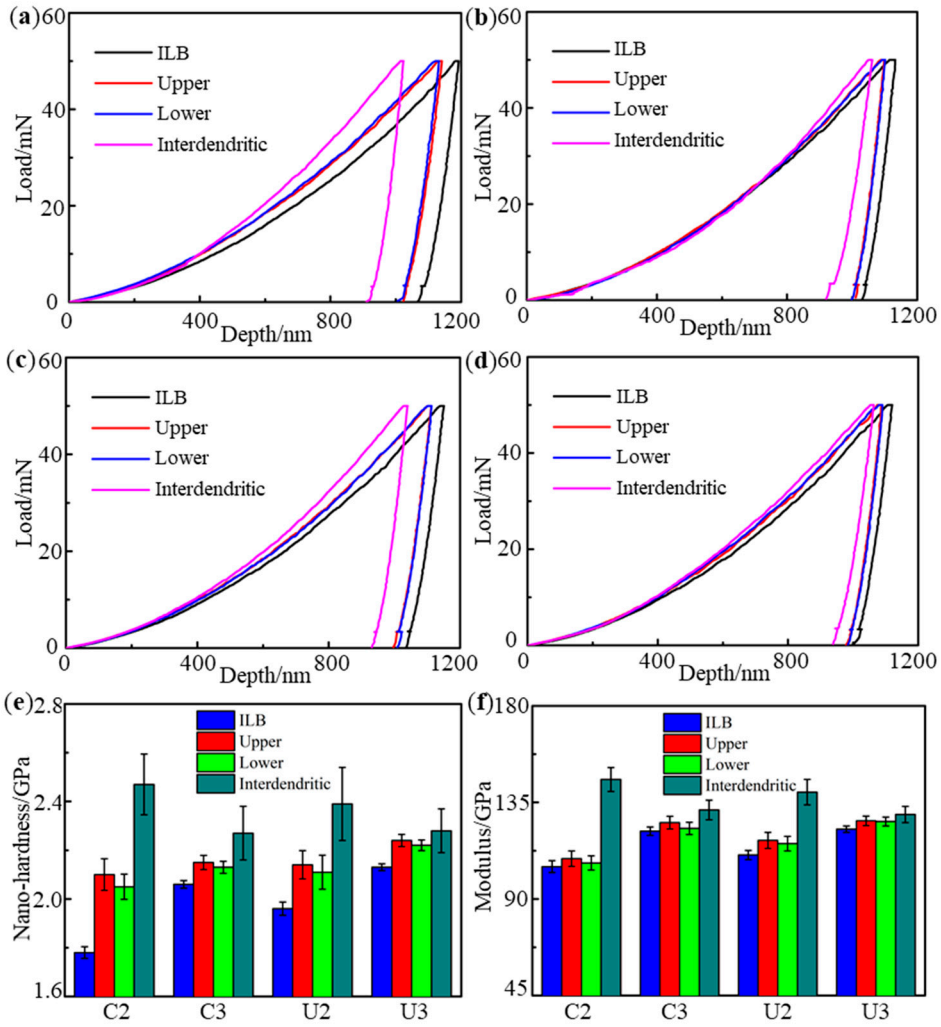

Figure 14. (**a**–**d**) Load-depth curves of C2, C3, U2 and U3, respectively, (**e**) nanohardness of C2, C3, U2 and U3, respectively, (**f**) modulus of C2, C3, U2 and U3, respectively.

Tensile properties of specimen U2, C3 and U3 are tested according to the effective area of deposition (Table 1) and the finer grain size (Figure 3). The typical stress-strain curves for the three conditions of the WAAM samples and cast C95220 alloys, as well as the tensile properties determine from these curves, are compared in Figure 15. It can be seen that all of the WAAM samples are found to exhibit considerably higher yield strength (YS) and elongation (EL) as compared to the cast samples. The cast C95220 alloys has higher ultimate tensile strength (UTS) than that of WAAM samples due to more contents of Al, Ni and Fe elements (the microstructure of C95220 alloys is shown in the inserted picture at the top left). The figures demonstrate that though the nature of the flow curves of the U2, C3 and U3 samples are similar, there is a marked difference in their properties. The yield strength of the U3 samples (224–227 MPa) are higher than that of the C3 (200–204 MPa) and U2 samples (189–193 MPa). In the perspective of NAB component engineering design, yield strength is more relevant than ultimate tensile strength. On the other hand, the ultimate tensile strength of U3 (515–518 MPa) samples are also higher than C3 (434–458 MPa) and U2 samples (387–438 MPa). The anisotropy of UTS exists in C3 and U2 samples. Regarding ductility, the elongation of U3 samples (40.56–41.42%) are comparable to that of the C3 samples (39.95–42.8%), while specimens prepared from U2 samples exhibit higher ductility (42.2–50.87%). The detailed results of the average tensile properties in the vertical direction (V) and horizontal direction (H) within the UTS, YS and EL are listed in Table 2.

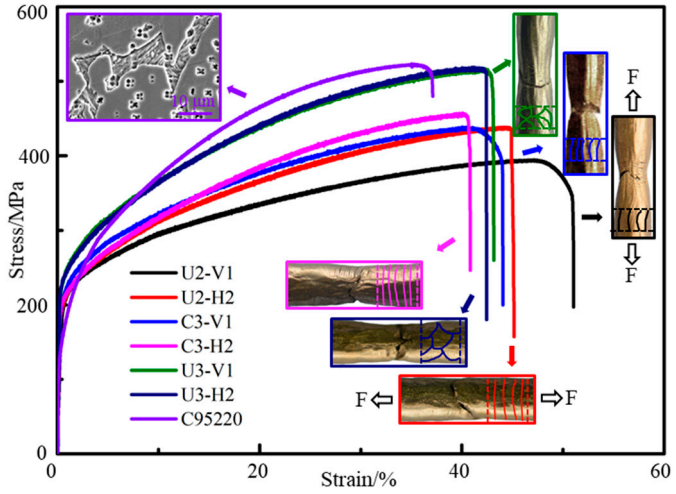

Figure 15. Comparison of stress-strain curves of cast C95220 alloys, U2, C3 and U3 samples (Inserted pictures represent the relationship between applying tension and grains direction in additive manufacturing samples, F means tensile force direction. Inserted picture at the top left is the microstructure of C95520 alloys).

Table 2. Tensile properties of the WAAM samples.

Direction	UTS/MPa	YS/MPa	EL/%
U2-V	390.3 ± 3.8	190.7 ± 1.0	48.9 ± 1.8
U2-H	430.1 ± 6.9	191.3 ± 0.8	43.1 ± 0.8
C3-V	436.5 ± 2.1	199.3 ± 0.9	42.1 ± 0.8
C3-H	454.9 ± 3.1	202.0 ± 1.3	40.5 ± 0.7
U3-V	516.1 ± 0.8	225.3 ± 0.9	40.9 ± 0.2
U3-H	517.5 ± 0.5	226.8 ± 0.5	41.2 ± 0.4

In order to study the interpass temperature and UVA treatment effects on different locations along the deposition direction on the tensile properties of the fabricated wall, the tensile properties at different heights along the deposition direction are tested. Experimental results are shown in Figure 16. In the U2 and C3 samples, the UTS is more sensitive to the locations within the build and decreasing along the build height. The near to substrate sample shows the highest UTS, which is caused by the finer microstructure in the bottom region. In addition, although the UTS of the samples at different heights differ, no clear trend can be identified in YS and ductility in the U2 and C3 samples. In addition, when a low interpass temperature of 100 °C is used, less decrease of UTS is generated along the deposited direction in C3 samples. After UVA treatment under an interpass temperature of 100 °C, the tensile properties of the samples at different heights tend to be stable. Hence, from both horizontal and vertical tensile properties consequences, it is considered that the tensile properties are symmetrical within the U3 samples. The UTS, YS, and EL of the U3 samples are 517.0 ± 0.89 MPa, 226.2 ± 0.95 MPa, and 41.01 ± 0.29%, respectively. Among all the test samples, anisotropy is well controlled in the samples with UVA treatment at an interpass temperature of 100 °C, and the increase of UTS and YS is not accompanied by any drop in the ductility.

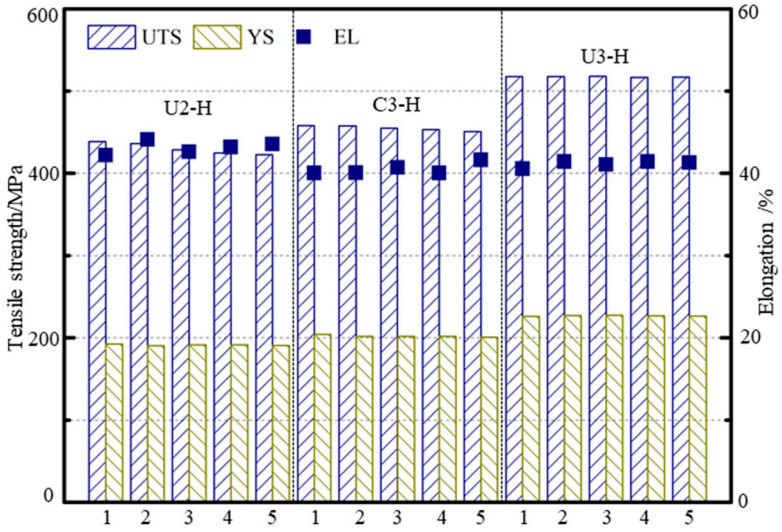

Figure 16. Effect of location on tensile properties and elongation of deposited metal in different regions of the corresponding Figure 1c.

Figure 17 shows that SEM micrographs of the tensile fracture surfaces for the Cu-8Al-2Ni-2Fe-2Mn alloy fabricated with and without UVA treatment under different interpass temperature. The fracture surface morphology of the U2 and C3 samples exhibits a transgranular ductile failure mode (Figure 17a–f). In U2-H direction samples, the slip separation (marked by the white arrow in Figure 17a,b) and dimples mix in the boundaries so that the PDA is clearly observed. The U2-V direction is mainly dominated by slip separation in fracture characteristics (Figure 17c). However, there are a large number of small and deep dimples aligned along the PAD boundaries when the UVA treatment is not applied (Figure 17d–f), implying a ductile type of fracture. With the UVA treatment under the interpass temperature of 100 °C, the grains sizes are greatly reduced, as grain boundaries become ambiguous in the fracture surface of the U3 samples and abundant finer dimples can be observed, as shown in Figure 17g–i, which also indicates a ductile failure mode. In addition, in the horizontal tensile fracture morphologies of the U2 and C3 samples, the PDA spacing in the fracture increases with different heights along the deposition direction, which is consistent with the results of microstructure observation (Figure 5) and also explains the tensile strength decreases with deposited height (Figure 16). The consistency of these tensile test results is in agreement with the changes in grain size observed in the microstructure, suggesting that UVA treatment under an interpass temperature of 100 °C is beneficial to the material properties of WAAM fabricated Cu-8Al-2Ni-2Fe-2Mn alloy components.

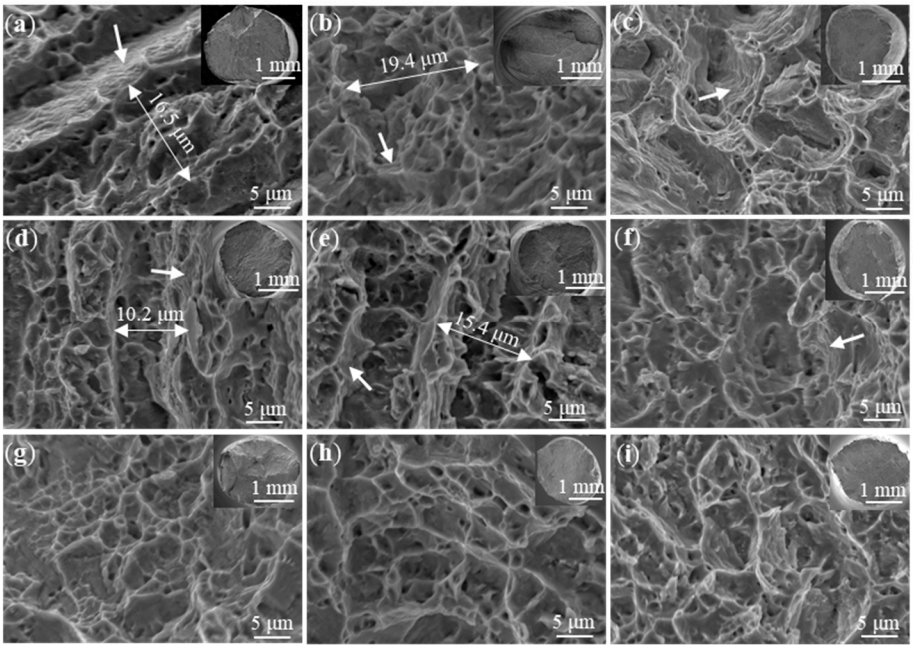

Figure 17. Fracture surfaces of tensile samples: (**a**) U2-H2, (**b**) U2-H4, (**c**) U2-V2, (**d**) C3-H2, (**e**) C3-H4, (**f**) C3-V2, (**g**) U3-H2, (**h**) U3-H4, (**i**) U3-V2. (The white arrow indicates the characteristics of slip separation).

It was found that the tensile properties are anisotropic between the horizontal and vertical directions in U2 and C3 samples. Previous studies have shown that the strength is related to the growth of columnar grains along the deposition direction [45]. Due to the different orientations of the tensile specimens, horizontal samples contain more grain boundaries, while the vertical samples contain more columnar grains (as shown the test samples pictures are inserted in Figure 15). Since the strength resulting from the grain boundaries is higher than the strength of the grains themselves, the strength of the horizontal tensile specimen is higher than the vertical one, and the elongation of the vertical sample is higher than that of the horizontal sample [46]. In addition, as the inserted test samples pictures are shown in Figure 15, the vertical samples show more obvious uniform elongation and necking when compared with the horizontal samples, which means vertical samples have greater plastic deformation and leading to a large amount of slip separations on the fracture (Figure 17c). As the strength increases and elongation decreases, fractures change to a mixture of slip separation and dimples (Figure 17a,b,d–f). In the U3 samples, the microstructure is cellular, and the relationship between the tensile force and grain boundaries is shown in Figure 15 (insert test samples pictures), where the number of dimples is increasing and the size is smaller than other samples.

Aside from the anisotropy of mechanical properties, when compared the U2 with C3 samples, the U3 sample fabricate with UVA treatment under an interpass temperature of 100 °C have remarkably larger tensile strength and yield strength. The mean values of these properties increase by 19.7% and 13.3% in UTS, and 15.8% and 11.1% in YS, respectively. In contrast, the elongation decreases by 9.4% in U2 samples, which is almost the same as elongation of C3 samples. The main factors contribute to higher strength are as follows: the grain refinement, the formation of twins and dislocations structure, and the presence of precipitating phase in α-Cu matrix. Firstly, it is clearly seen that U3 samples have fine grains than other parameters samples (Figures 3 and 5). This fine cellular structure is the direct outcome of UVA treatment under an interpass temperature of 100 °C and is observed in many other UVA treatments for manufacturing of processed materials [25]. The grain size reduced significantly, and the material is strengthened according to the Hall-Petch effect [47]. Further, Wang et al. [48] also made it clear that the fine cellular structure significantly enhanced the strength of additive manufacturing samples. Secondly, due to the UVA treatment WAAM process, the twins and dislocations form,

coherent twins have a strengthening effect that is similar to the influence of grain boundaries [41]. The generated twins act as additional grain boundaries and interrupt dislocation gliding, resulting in the dynamic Hall-Petch effect [49]. Thirdly, the results of TEM confirm the existence of the precipitate κ_{IV} phase in the α-Cu matrix (Figure 9). The precipitates are bypassed through the dislocation looping mechanism, which increases in strength [41]. It may be noted that the WAAM process under UVA at an interpass temperature of 100 °C probably restricts the solid-state transformation of κ_{IV} phase due to more superior cooling rates. However, in fact, this process may reduce the formation of interdendritic (more κ_{II} phase, composed of Fe-rich), and promote the distribution of Fe into the α-Cu matrix. During the WAAM process, the previous layers are subjected to re-heating by the thermal cycle of the subsequent deposition. The temperature range of 500 to 600 °C would result in homogeneous κ_{IV} precipitation in the α-Cu matrix [17]. In this temperature range, the WAAM process has a significant reduction in cooling rate and this condition can be retained for a long time (Figure 7b), and when Fe is sufficient, more κ_{IV} phase will precipitate in α-Cu matrix. Moreover, it can maintain good ductility in U3 sample that is fabricated by UVA treatment WAAM under interpass temperature of 100 °C methods could be mainly due to the formation of cellular structure [42]. Furthermore, the fact that the fracture morphology develops from the slip separation of high interpass temperature to fine dimples at the lower interpass temperature, which also verify the general trend of increasing strength and keep ductility. In addition, compared with the U2 samples, the tensile strength of the C3 samples increase slightly, which mainly results in the refinement of the columnar dendrites.

4. Conclusions

In this study, the effects of interpass temperature and ultrasonic vibration on microstructural characteristics (including the macrostructure, microstructure, elemental distribution, and phase composition) and mechanical properties (including nano-hardness and tensile strength) of WAAM fabricated Cu-8Al-2Ni-2Fe-2Mn parts are investigated. The results are as follows:

(1) Interpass temperatures of 100 °C and 400 °C have no significant effect on the microstructural feature. The alloy fabricated under different interpass temperatures without UVA treatment is mainly composed of the columnar dendrites growing epitaxially along the deposition direction.

(2) The microstructure of the Cu-8Al-2Ni-2Fe-2Mn alloy is refined by ultrasonic vibration. With the UVA treatment process, continuous directional growth of columnar dendrites is broken at the interpass temperature of 400 °C, and forms cellular structure at the interpass temperature of 100 °C. A comparison of parts not treated by UVA and parts treated by UVA at 400 °C indicates that parts treated by UVA at 100 °C have a smaller grain size and better material dispersion.

(3) With UVA treatment at the interpass temperature of 100 °C, the alloy has an interdendritic microstructure containing globular κ_{II} phase based on Fe_3Al and lamellar κ_{III} phase based on NiAl, whereas precipitates κ_{IV} phase (rich-Fe) is nucleated in the α-Cu matrix. The twinning and dislocation have been observed in the UVA treatment alloy.

(4) The nano-hardness and modulus of interdendritic and α-Cu matrix are different at interpass temperature of 400 °C, and the nano-hardness and modulus of interdendritic are higher. The nano-hardness and modulus of the α-Cu matrix increases as the interpass temperature decreases. In the UVA treatment at the interpass temperature of 100 °C, the nano-hardness and modulus are more uniform, the nano-hardness ranges from 2.11 to 2.28 GPa while the modulus ranges from 122.4 to 129.4 GPa.

(5) Tensile properties are anisotropic at interpass temperature of 100 °C and UVA treatment at an interpass temperature of 400 °C. In the UVA treatment at an interpass temperature of 100 °C, it displays almost isotropic tensile properties and obtaines the best strength-ductility combinations. The UTS, YS, and EL are 517.0 ± 0.89 MPa, 226.2 ± 0.95 MPa and 41.01 ± 0.29%, respectively. Two typical fracture characteristics, i.e., slip separation occurs at high interpass temperature, and it is mainly a dimple feature at a low interpass temperature.

Author Contributions: Methodology, W.C. and T.W.; writing—original draft preparation, W.C.; writing—review and editing, Y.C. and T.Z.; funding acquisition, Y.C.; data curation, Z.Y.; conceptualization, Y.C. and X.F. All authors have read and agreed to the published version of the manuscript.

Funding: This paper was supported by the National Defense Basic Research Program grant number JCKY2018401C003; Key Research and Development Project of Jiangxi Province grant number 20192BBH80018; Jiangxi Distinguished Young Scholars grant number 2018ACB21016; Jiangxi Advantageous Scientific and Technological Innovation Team grant number 20171BCB24007.

Conflicts of Interest: The authors declare no conflict of interest.

References

1. Ding, Y.; Zhao, R.; Qin, Z.; Wu, Z.; Wang, L.; Liu, L.; Lu, W. Evolution of the corrosion product film on nickel-aluminum bronze and its corrosion behavior in 3.5 wt % NaCl solution. *Materials* **2019**, *12*, 209. [CrossRef]
2. Fonlupt, S.; Bayle, B.; Delafosse, D.; Heuze, J. Role of second phases in the stress corrosion cracking of a nickel-aluminium bronze in saline water. *Corros. Sci.* **2005**, *47*, 2792–2806. [CrossRef]
3. Rahni, M.R.M.; Beidokhti, B.; Haddad-sabzevar, M. Effect of filler metal on microstructure and mechanical properties of manganese–aluminum bronze repair welds. *Trans. Nonferrous Met. Soc. China* **2017**, *27*, 507–513. [CrossRef]
4. Lv, Y.; Wang, L.; Han, Y.; Xu, X.; Lu, W. Investigation of microstructure and mechanical properties of hot worked NiAl bronze alloy with different deformation degree. *Mater. Sci. Eng. A* **2015**, *643*, 17–24. [CrossRef]
5. Culpan, E.A.; Rose, G. Microstructural characterization of cast nickel aluminium bronze. *J. Mater. Sci.* **1978**, *13*, 1647–1657. [CrossRef]
6. Hasan, F.; Jahanafrooz, A.; Lorimer, G.W.; Ridley, N. The morphology, crystallography, and chemistry of phases in as-cast nickel-aluminum bronze. *Metall. Trans. A* **1982**, *13*, 1337–1345. [CrossRef]
7. Nelson, E. Microstructural Effects of Multiple Passes during Friction stir Processing of Nickel Aluminum Bronze. Master's Thesis, Naval Postgraduate School, Monterey, CA, USA, December 2009.
8. Hasan, F.; Lorimer, G.; Ridley, N. Crystallography of martensite in a Cu-10Al-5Ni-5Fe alloy. *J. Phys.* **1982**, *43*, 653–658. [CrossRef]
9. Wharton, J.A.; Barik, R.C.; Kear, G.; Wood, R.J.K.; Stokes, K.R.; Walsh, F.C. The corrosion of nickel-aluminium bronze in seawater. *Corros. Sci.* **2005**, *47*, 3336–3367. [CrossRef]
10. Rodrigues, T.; Duarte, V.; Miranda, R.M.; Santos, T.; Oloveira, J.P. Current status and perspectives on wire and arc additive manufacturing (WAAM). *Materials* **2019**, *12*, 1121. [CrossRef] [PubMed]
11. Köhler, M.; Fiebig, S.; Hensel, J.; Dilger, K. Wire and arc additive manufacturing of aluminum components. *Metals* **2019**, *9*, 608. [CrossRef]
12. Li, Z.; Cui, Y.; Wang, J.; Liu, C.; Wang, J.; Xu, T.; Lu, T.; Zhang, H.; Lu, J.; Ma, S.; et al. Characterization of microstructure and mechanical properties of stellite 6 part fabricated by wire arc additive manufacturing. *Metals* **2019**, *9*, 474. [CrossRef]
13. Bai, X.; Colegrove, P.; Ding, J.; Zhou, X.; Diao, C.; Bridgeman, P.; Hönnige, J.R.; Zhang, H.; Williams, S. Numerical analysis of heat transfer and fluid flow in multilayer deposition of PAW-based wire and arc additive manufacturing. *Int. J. Heat Mass Transf.* **2018**, *124*, 504–516. [CrossRef]
14. Fachinotti, V.D.; Cardona, A.; Baufeld, B.; Biest, O.V. Finite-element modelling of heat transfer in shaped metal deposition and experimental validation. *Acta Mater.* **2012**, *60*, 6621–6630. [CrossRef]
15. Ding, D.; Pan, Z.; Duin, S.; Li, H.; Shen, C. Fabricating superior NiAl bronze components through wire arc additive manufacturing. *Materials* **2016**, *9*, 652. [CrossRef] [PubMed]
16. Shen, C.; Pan, Z.; Ding, D.; Yuan, L.; Nie, N.; Wang, Y.; Luo, D.; Cuiuri, D.; Duin, S.; Li, H. The influence of post-production heat treatment on the multi-directional properties of nickel-aluminum bronze alloy fabricated using wire-arc additive manufacturing process. *Add. Manuf.* **2018**, *23*, 411–421. [CrossRef]
17. Dharmendra, C.; Hadadzadeh, A.; Amirkhiz, B.S.; Ram, G.D.; Mohammadi, M. Microstructural evolution and mechanical behavior of nickel aluminum bronze Cu-9Al-4Fe-4Ni-1Mn fabricated through wire-arc additive manufacturing. *Add. Manuf.* **2019**, *30*, 100872. [CrossRef]
18. Komarov, S.; Kuwabara, M.; Abramov, V. High power ultrasonics in pyrometallurgy: current status and recent development. *ISIJ Int.* **2005**, *45*, 1765–1782. [CrossRef]

19. Zhao, Y.; Lin, B.; Song, D.; Zheng, D.; Sun, Z.; Xie, C.; Zhang, W. Effect of compound fields of ultrasonic vibration and applied pressure on the 3D microstructure and tensile properties of recycled Al-Cu-Mn-Fe-Si alloys. *Materials* **2019**, *12*, 3904. [CrossRef] [PubMed]
20. Huang, K.; Jiang, R.; Li, X.; Zhang, L.; Li, Z.; Li, R. Effects of high-intensity ultrasound on microstructure and mechanical property of in situ TiB_2/2A14 composites. *Metals* **2019**, *9*, 1210. [CrossRef]
21. Chen, Q.; Ge, H.; Yang, C.; Lin, S.; Fan, C. Study on pores in ultrasonic-assisted TIG weld of aluminum alloy. *Metals* **2017**, *7*, 53. [CrossRef]
22. Li, M.; Zhang, Q.; Han, B.; Song, L.; Cui, G.; Yang, J.; Li, J. Microstructure and property of Ni/WC/La_2O_3 coatings by ultrasonic vibration-assisted laser cladding treatment. *Opt. Lasers Eng.* **2020**, *125*, 105848. [CrossRef]
23. Ning, F.; Cong, W. Microstructures and mechanical properties of Fe-Cr stainless steel parts fabricated by ultrasonic vibration-assisted laser engineered net shaping process. *Mater. Lett.* **2016**, *179*, 61–64. [CrossRef]
24. Yang, Y.; Jin, X.; Liu, C.; Xiao, M.; Lu, J.; Fan, H.; Ma, S. Residual stress, mechanical properties, and grain morphology of Ti-6Al-4V alloy produced by ultrasonic impact treatment assisted wire and arc additive manufacturing. *Metals* **2018**, *8*, 934. [CrossRef]
25. Wang, H.; Hu, Y.; Ning, F.; Cong, W. Ultrasonic vibration-assisted laser engineered net shaping of Inconel 718 parts: Effects of ultrasonic frequency on microstructural and mechanical properties. *J. Mater. Process. Technol.* **2020**, *276*, 116395. [CrossRef]
26. Zhang, Y.; Guo, Y.; Chen, Y.; Kang, L.; Cao, Y.; Qi, H.; Yang, S. Ultrasonic–assisted laser metal deposition of the Al 4047alloy. *Metals* **2019**, *9*, 1111. [CrossRef]
27. Wang, J.F.; Sun, Q.J.; Wang, H.; Liu, J.P.; Feng, J.C. Effect of location on microstructure and mechanical properties of additive layer manufactured Inconel 625 using gas tungsten arc welding. *Mater. Sci. Eng. A* **2016**, *676*, 395–405. [CrossRef]
28. David, S.A.; Babu, S.S.; Vitek, J.M. Welding: solidification and microstructure. *JOM* **2003**, *55*, 14–20. [CrossRef]
29. Hunt, J.D. Steady state columnar and equiaxed growth of dendrites and eutectic. *Mater. Sci. Eng.* **1984**, *65*, 75–83. [CrossRef]
30. Li, Q.; Lin, X.; Liu, F.; Liu, F.; Huang, W. Microstructural characteristics and mechanical properties of laser solid formed K465 superalloy. *Mater. Sci. Eng. A* **2017**, *700*, 649–655. [CrossRef]
31. Liu, J.; Zhu, H.; Li, Z.; Cui, W.; Shi, Y. Effect of ultrasonic power on porosity, microstructure, mechanical properties of the aluminum alloy joint by ultrasonic assisted laser–MIG hybrid welding. *Opt. Lasers. Eng.* **2019**, *119*, 105619. [CrossRef]
32. Kang, J.; Zhang, X.; Wang, S.; Ma, J.; Huang, T. The comparison of ultrasonic effects in different metal melts. *Ultrasonics* **2015**, *57*, 11–17. [CrossRef]
33. Eskin, G.I. Broad prospects for commercial application of the ultrasonic (cavitation) melt treatment of light alloys. *Ultrason. Sonochem.* **2001**, *8*, 319–325. [CrossRef]
34. Zhu, Y.; Tian, X.; Li, J.; Wang, H. Microstructure evolution and layer bands of laser melting deposition Ti–6.5Al–3.5Mo–1.5Zr–0.3Si titanium alloy. *J. Alloys Compd.* **2014**, *616*, 468–474. [CrossRef]
35. Ho, A.; Zhao, H.; Fellowes, J.; Martina, F.; Davis, A.; Prangnell, P. On the origin of microstructural banding in Ti–6Al4V wire–arc based high deposition rate additive manufacturing. *Acta Mater.* **2019**, *166*, 306–323. [CrossRef]
36. Kurz, W.; Fisher, D.J. *Fundamentals of Solidification*, 4th ed.; Trans Tech Publications Ltd.: Stafa-Zurich, Switzerland, 1998; pp. 86–91.
37. Bermingham, M.J.; StJohn, D.H.; Krynen, J.; Tedman-Jones, S.; Dargush, M.S. Promoting the columnar to equiaxed transition and grain refinement of titanium alloys during additive manufacturing. *Acta Mater.* **2019**, *168*, 261–274. [CrossRef]
38. Humphreys, F.J.; Ardakani, M.G. Grain boundary migration and Zener pinning in particle–containing copper crystals. *Acta Mater.* **1996**, *44*, 2717–2727. [CrossRef]
39. Nie, K.B.; Wang, X.J.; Hu, X.S.; Xu, L.; Wu, K.; Zheng, M.Y. Microstructure and mechanical properties of SiC nanoparticles reinforced magnesium matrix composites fabricated by ultrasonic vibration. *Mater. Sci. Eng. A* **2011**, *528*, 5278–5282. [CrossRef]
40. Liu, J.; Suslov, S.; Ren, Z.; Dong, Y.; Ye, C. Microstructure evolution in Ti64 subjected to laser-assisted ultrasonic nanocrystal surface modification. *Int. J. Mach. Tools Manuf.* **2019**, *136*, 19–33. [CrossRef]

41. Wen, H.; Topping, T.; Isheim, D.; Seidman, D.; Lavernia, E. Strengthening mechanisms in a high–strength bulk nanostructured Cu-Zn-Al alloy processed via cryomilling and spark plasma sintering. *Acta Mater.* **2013**, *61*, 2769–2782. [CrossRef]
42. Lu, L.; Chen, X.; Huang, X.; Lu, K. Revealing the maximum strength in nanotwinned copper. *Science* **2009**, *323*, 607–610. [CrossRef]
43. Seok, M.Y.; Choi, I.C.; Moon, J.; Kim, S.; Ramamurty, U.; Jang, J. Estimation of the Hall–Petch strengthening coefficient of steels through nanoindentation. *Scr. Mater.* **2014**, *87*, 49–52. [CrossRef]
44. Cook, M.; Fentiman, W.P.; Davis, E. Observations on the structure and properties of wrought copper–aluminium-nickel-iron alloys. *J. Inst. Met.* **1951**, *80*, 419–429.
45. Carroll, B.E.; Palmer, T.A.; Beese, A.M. Anisotropic tensile behavior of Ti-6Al-4V components fabricated with directed energy deposition additive manufacturing. *Acta Mater.* **2015**, *87*, 309–320. [CrossRef]
46. Shen, C.; Pan, Z.; Cuiuri, D.; Dong, B.; Li, H. In–depth study of the mechanical properties for Fe_3Al based iron aluminide fabricated using the wire–arc additive manufacturing process. *Mater. Sci. Eng. A* **2016**, *669*, 118–126. [CrossRef]
47. Fu, H.H.; Benson, D.J.; Meyers, M.A. Analytical and computational description of effect of grain size on yield stress of metals. *Acta Mater.* **2001**, *49*, 2567–2582. [CrossRef]
48. Wang, Y.M.; Voisin, T.; Mckeown, J.; Ye, J.; Calta, N.; Li, Z.; Zeng, Z.; Zhang, Z.; Chen, W.; Roehling, T.T.; et al. Additively manufactured hierarchical stainless steels with high strength and ductility. *Nat. Mater.* **2018**, *17*, 63–71. [CrossRef]
49. Balogh, L.; Ungár, T.; Zhao, Y.; Zhu, Y.T.; Horita, Z.; Xu, C.; Langdon, T. Influence of stacking–fault energy on microstructural characteristics of ultrafine-grain copper and copper-zinc alloys. *Acta Mater.* **2008**, *56*, 809–820. [CrossRef]